

J-freezing and Hund's rules in spin-orbit-coupled multiorbital Hubbard models

Aaram J. Kim,^{1,*} Harald O. Jeschke,¹ Philipp Werner,² and Roser Valentí¹

¹*Institut für Theoretische Physik, Goethe-Universität Frankfurt,
Max-von-Laue-Str. 1, 60438 Frankfurt am Main, Germany*

²*Department of Physics, University of Fribourg, Chemin du Musée 3, 1700 Fribourg, Switzerland*

We investigate the phase diagram of the spin-orbit-coupled three orbital Hubbard model at arbitrary filling by means of dynamical mean-field theory combined with continuous-time quantum Monte Carlo. We find that the spin-freezing crossover occurring in the metallic phase of the non-relativistic multiorbital Hubbard model can be generalized to a **J**-freezing crossover, with $\mathbf{J} = \mathbf{L} + \mathbf{S}$, in the spin-orbit-coupled case. In the **J**-frozen regime the correlated electrons exhibit a non-trivial flavor selectivity and energy dependence. Furthermore, in the regions near $n = 2$ and $n = 4$ the metallic states are qualitatively different from each other, which reflects the atomic Hund's third rule. Finally, we explore the appearance of magnetic order from exciton condensation at $n = 4$ and discuss the relevance of our results for real materials.

PACS numbers: 71.10.Hf, 71.15.Rf, 71.30.+h, 75.25.Dk

Introduction. In 4d and 5d transition metal oxides the interplay and competition between kinetic energy, spin-orbit coupling (SOC) and correlation effects results in several interesting phenomena, such as spin-orbit assisted Mott transitions [1–6], unconventional superconductivity [9, 10], topological phases [11], exciton condensation [10, 12, 13], or exotic magnetic orders [14, 15]. Transition metal oxides involving 4d and 5d electrons show diverse structures like the Ruddlesden-Popper series [1, 9], double perovskite, [14–16] two-dimensional honeycomb geometry [3–8] or pyrochlore lattices [17]. In an octahedral environment, as in most of the 4d and 5d materials mentioned above, the five d orbitals are split into low energy t_{2g} and higher energy e_g levels. The SOC further splits the low energy t_{2g} levels into a so-called $j = 1/2$ doublet and $j = 3/2$ quadruplet. The energy separation between the $j = 1/2$ and $j = 3/2$ bands is proportional to the strength of the SOC. Existing *ab-initio* density functional theory calculations [17, 18] suggest that in some materials a multiorbital description including both the $j = 1/2$ and $j = 3/2$ subbands should be considered.

Most theoretical studies of 4d and 5d systems have focused on material-specific models with fixed electronic filling. Here we follow a different strategy and explore the possible states that emerge from a multiband Hubbard model with spin-orbit coupling at arbitrary filling. This allows us to investigate unexplored regions in parameter space which may exhibit interesting phenomena. Specifically, by performing a systematic analysis of the local **J** moment susceptibility ($\mathbf{J} = \mathbf{L} + \mathbf{S}$) as a function of Coulomb repulsion U , Hund's coupling J_H , spin-orbit coupling λ and filling n , we identify Mott-Hubbard insulating phases and complex metallic states. We find a **J**-freezing crossover between a Fermi liquid (FL) and a non-Fermi liquid (NFL) phase where the latter shows a distinct flavor selectivity that originates from the SOC. In addition, we observe a strong asymmetry in the metallic phase between filling $n = 2$ and $n = 4$ with properties

reminiscent of the atomic Hund's third rule. Finally, we investigate doping effects on the excitonic magnetism at $n = 4$.

Method. We consider a three-orbital Hubbard model with spin-orbit coupling. The model Hamiltonian consists of three terms,

$$\mathcal{H} = \mathcal{H}_t + \mathcal{H}_\lambda + \mathcal{H}_U, \quad (1)$$

where \mathcal{H}_t , \mathcal{H}_λ , and \mathcal{H}_U denote the electron hopping, spin-orbit coupling, and local Coulomb interaction terms, respectively. In order to discuss the underlying physics, relevant for a range of materials with different structures, we use a semi-circular density of states (DOS), $\rho^0(\omega) = (2/\pi D)\sqrt{1 - (\omega/D)^2}$ for all orbitals. The half-bandwidth D is set to unity. \mathcal{H}_λ is constructed by projecting the SOC term of d orbitals onto the t_{2g} subspace,

$$\mathcal{H}_\lambda = \lambda \sum_{\substack{\alpha\beta \\ \sigma\sigma'}} c_{i\alpha\sigma}^\dagger \langle \alpha\sigma | \mathcal{P}_{t_{2g}} \mathbf{L}^d \mathcal{P}_{t_{2g}} \cdot \mathbf{S} | \beta\sigma' \rangle c_{i\beta\sigma'}, \quad (2)$$

where $\mathcal{P}_{t_{2g}}$ is the projection operator. $c_{i\alpha\sigma}$ ($c_{i\alpha\sigma}^\dagger$) denotes the annihilation (creation) operator of a spin σ electron at site i and orbital α . The angular momentum operator within the t_{2g} subspace can be represented by an effective $L = 1$ angular momentum operator with an extra minus sign [14].

The local Coulomb interaction Hamiltonian is written in Kanamori form [19] including the spin-flip and pair-hopping terms as:

$$\begin{aligned} \mathcal{H}_U = & U \sum_{i,\alpha} n_{i\alpha\uparrow} n_{i\alpha\downarrow} + \sum_{i,\alpha < \alpha'} (U' - J_H \delta_{\sigma\sigma'}) n_{i\alpha\sigma} n_{i\alpha'\sigma'} \\ & - J_H \sum_{i,\alpha < \alpha'} (c_{i\alpha\uparrow}^\dagger c_{i\alpha'\downarrow}^\dagger c_{i\alpha'\uparrow} c_{i\alpha\downarrow} + h.c.) \\ & + J_H \sum_{i,\alpha < \alpha'} (c_{i\alpha\uparrow}^\dagger c_{i\alpha\downarrow}^\dagger c_{i\alpha'\downarrow} c_{i\alpha'\uparrow} + h.c.) . \end{aligned} \quad (3)$$

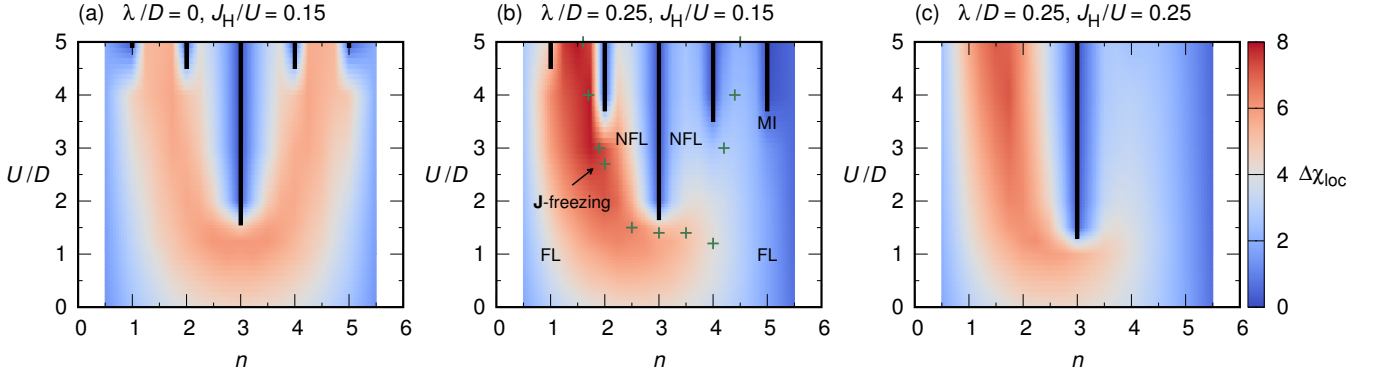


FIG. 1. Dynamic contribution to the local susceptibility, $\Delta\chi_{\text{loc}}$ in the $(U/D, n)$ phase diagram for (a) $\lambda/D = 0.0$, $J_H/U = 0.15$, (b) $\lambda/D = 0.25$, $J_H/U = 0.15$, (c) $\lambda/D = 0.25$, $J_H/U = 0.25$, and $T/D = 0.03$. Cross symbols mark the maximum values of $\Delta\chi_{\text{loc}}$ corresponding to the **J**-freezing crossover points. The parameter set for (b) is chosen by following the tight-binding parameters of Sr_2IrO_4 [20]. The reported values of the λ , J_H , and U for various materials are summarized in the supplementary material.

Here, U is the on-site Coulomb interaction and J_H denotes the Hund's coupling. U' is set to $U - 2J_H$ to make the interaction rotationally invariant in orbital space.

We employ the dynamical mean-field theory (DMFT) [21] to solve the model Hamiltonian Eq. (1) in a broad parameter space. Since DMFT is a non-perturbative technique within the local self-energy approximation, we can access metallic and insulating phases on the same footing. In addition, the dynamical fluctuations encoded in the DMFT solution contain valuable information on the degree of moment correlations and the corresponding susceptibility. We will use the local **J** moment susceptibility as a central quantity to investigate the phase diagram.

As an impurity solver, we adopt the continuous-time quantum Monte Carlo method (CTQMC) in the hybridization expansion variant [22, 23]. For the single particle basis of the CTQMC calculation, we choose the relativistic j effective basis ($j = 1/2$, $j = 3/2$) which is an eigenbasis of the SOC Hamiltonian. It was previously reported that the j effective basis reduces the sign problem of the CTQMC simulation [24]. For symmetry broken phases, we consider the off-diagonal hybridization functions.

Results. A strong Coulomb interaction localizes electrons and can lead to the formation of local moments. The freezing of these local moments is signaled by a slow decay, and eventual saturation, of the dynamical correlation function $\langle J_z(\tau)J_z(0) \rangle$ on the imaginary-time axis. Hence, the local susceptibility, defined as

$$\chi_{\text{loc}} = \int_0^\beta d\tau \langle J_z(\tau)J_z(0) \rangle, \quad (4)$$

allows us to investigate the formation and freezing of local moments. In addition, we define the dynamical contribution to the local susceptibility by eliminating the long-term memory of the correlation function from the

original χ_{loc} [25]:

$$\Delta\chi_{\text{loc}} = \int_0^\beta d\tau \left(\langle J_z(\tau)J_z(0) \rangle - \langle J_z(\beta/2)J_z(0) \rangle \right). \quad (5)$$

As the system evolves from an itinerant to a localized phase, $\Delta\chi_{\text{loc}}$ exhibits a maximum in the intermediate Coulomb interaction regime (see Fig. S1(c,d) in Ref. [26]); both, (i) the enhanced correlations compared to the non-interacting limit and (ii) the larger fluctuations compared to the localized limit lead to the maximum in $\Delta\chi_{\text{loc}}$. The location of the $\Delta\chi_{\text{loc}}$ maxima in the phase diagram can be viewed as the boundary of the local moment regime and has been used to define the ‘spin-freezing crossover line’ in the non-spin-orbit coupled system [25, 33]. However, since spin is not a good quantum number in the spin-orbit-coupled system, we introduce the total moment $\mathbf{J} = \mathbf{S} + \mathbf{L}$ to generalize the ‘spin-freezing’ to a ‘**J**-freezing’ crossover.

In the following, we discuss the paramagnetic phase diagram of Eq. (1) obtained with DMFT(CTQMC) as a function of U , J_H , λ and n . Figures 1 (a-c) show contour plots of $\Delta\chi_{\text{loc}}$ in the interaction vs. filling plane for three different parameter sets of λ and J_H . Since SOC breaks particle-hole symmetry, Fig. 1 (b), (c) are not symmetric about the half-filling axis, $n = 3$. The Mott insulating phase (black lines in Fig. 1) which we identify as the region where the spectral function vanishes at the Fermi-level and where $\Delta\chi_{\text{loc}}$ is smallest, appears at each commensurate filling. Nonetheless, compared to the system without SOC (Fig. 1 (a)), the change of the critical interaction strength U_c shows a complex behavior depending on the filling and λ . We can quantitatively analyze the change of U_c using the Mott-Hubbard criterion, according to which a Mott transition occurs when the atomic charge gap becomes comparable to the average kinetic

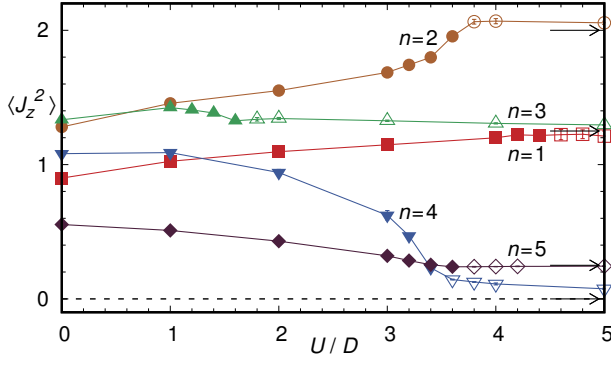


FIG. 2. Size of the local J_z -moments as a function of interaction strength U/D for $\lambda/D = 0.25$, $J_H/U = 0.15$ and $T/D = 0.03$ at various commensurate fillings. The parameter set is the same as in Fig. 1(b). Solid (Open) symbols correspond to the metallic (insulating) solutions. The arrows represent the corresponding values from the Hund's rule.

energy:

$$\Delta_{\text{ch}}(n, U_c, J_H, \lambda) \equiv U_c + \delta\Delta_{\text{ch}}(n, J_H, \lambda) = \tilde{W}(n, J_H, \lambda). \quad (6)$$

Δ_{ch} is the charge gap of the local Hamiltonian, and $\tilde{W}(n, J_H, \lambda)$ is the average kinetic energy. Here, n is integer for commensurate Mott insulators. Since SOC reduces the degeneracy of the atomic ground states, \tilde{W} is basically a decreasing function of λ except for $n = 3$ where the ground state degeneracy is not changed by introducing SOC. By diagonalizing the local Hamiltonian, we observe that $\delta\Delta_{\text{ch}}$ is an increasing function of λ for $n = 1, 2$, and 4 , but a decreasing function for $n = 3$ and 5 . Altogether, for $n = 1, 2$, and 4 , the two terms contributing to $U_c = \tilde{W} - \delta\Delta_{\text{ch}}$ cooperate to reduce U_c as we also observe in our DMFT results. A smaller U_c at $n = 4$ compared to $n = 2$ is consistent with the Mott-Hubbard criterion. In contrast, for $n = 5$ the two contributions to U_c compete and it is hard to predict the behavior of U_c from this criterion. We can anticipate based on the DMFT results that the reduction of the kinetic energy dominates the slight decrease of the atomic gap. Finally, at $n = 3$ there is an unchanged degeneracy and $\delta\Delta_{\text{ch}}$ decreases due to SOC implying a slight increase of U_c (compare Fig. 1 (a) and (b) and see Fig. S4 in Ref. 26).

The effect of the Hund's coupling can be seen by comparing Figs. 1 (b) and (c). Away from half-filling, U_c increases with J_H but at half-filling it slightly decreases, which is consistent with the behavior of $\delta\Delta_{\text{ch}}$ [34]. For even stronger SOC, $\lambda/D = 0.5$, a drastically reduced U_c is found at $n = 4$ implying an adiabatic connection of the Mott insulator to the band insulator in the $\lambda \gg 1$ limit [26, 35].

We now concentrate on the metallic regions. In the spin-orbit-coupled multi-orbital system the dynamic contribution to the susceptibility is larger below half-filling compared to the particle-hole transformed state (red area

in Fig. 1 (b) and (c)). Such a difference mainly comes from the cross-correlation between the spin and the orbital moment, which is positive for $n < 3$ and negative for $n > 3$ (see Fig. S3(d) in [26]). A recent study [25] has shown that in the case of a multi-orbital Hubbard model without spin-orbit coupling, s -wave spin-triplet superconductivity can appear along the spin-freezing line. The effect of the spin-orbital cross-correlation on this superconductivity will be an interesting future research topic.

The asymmetry in susceptibility and dynamical contribution to the susceptibility between below and above half-filling can be explained by Hund's third rule whose origin is the spin-orbit coupling [26, 36, 37]. Following Hund's third rule, in the atomic limit the alignment between \mathbf{L} and \mathbf{S} depends on whether the filling is below or above half-filling. In our calculation, \mathbf{L} and \mathbf{S} are aligned in the same direction below half-filling, while they are anti-aligned above half-filling. Therefore, the size of the total \mathbf{J} -moment is larger at fillings below $n = 3$ as we increase the interaction strength and further localize the electrons. Figure 2 shows the evolution of $\langle J_z^2 \rangle$ as a function of Coulomb interaction strength for five commensurate fillings and parameter values as chosen in Fig. 1 (b). In the intermediate and strong interaction region, $U/D \gtrsim 2$, an enhanced value of the \mathbf{J} -moment is found at $n = 2$ and 1 compared to the cases $n = 4$ and 5 , respectively. In the strong correlation (Mott insulating) regime, the alignment of the spin, orbital, and \mathbf{J} -moment is consistent with the atomic results according to Hund's rules. The \mathbf{J} -moment determined by atomic Hund's rule has strong effect on the $\Delta\chi_{\text{loc}}$ and χ_{loc} in the metallic phase even at moderate U values.

Inside the \mathbf{J} -freezing region (denoted by crosses in Fig. 1 (b)), we observe a non-Fermi liquid (NFL) behavior of the metallic state. In order to explore this state we show in Figs. 3 (a) and (b) the imaginary part of the self-energy on the Matsubara frequency axis across the \mathbf{J} -freezing crossover line for the same parameter values as in Fig. 1 (b) and various fillings. In the low frequency region, $\text{Im} \Sigma(i\omega_n)$ can be expressed in the form $-\Gamma - C\omega_n^\alpha$. As we cross the \mathbf{J} -freezing line, (region between $n \simeq 2$ and $n \simeq 4$ for $U = 3$) Γ changes from zero to a finite value indicating a Fermi-liquid (FL) to NFL crossover. Near the \mathbf{J} -freezing line, a small Γ value with a non-integer exponent α is found.

These two characteristic properties of the FL to NFL crossover are reminiscent of the spin-freezing crossover observed in the model without SOC [33]. As the system gets closer to $n = 3$, the correlation function $\langle S_z(\tau)S_z(0) \rangle$ increases while that of $\langle L_z(\tau)L_z(0) \rangle$ and $\langle L_z(\tau)S_z(0) \rangle$ decreases in magnitude [26], so that the orbitally averaged scattering rate is determined primarily by the frozen spin moments. However, due to SOC, the self-energy $\text{Im} \Sigma(i\omega_n)$ of the $j = 1/2$ electron is different from that of the $j = 3/2$ electrons. At low frequency, the difference between $j = 1/2$ and $3/2$ is enhanced in the NFL phase

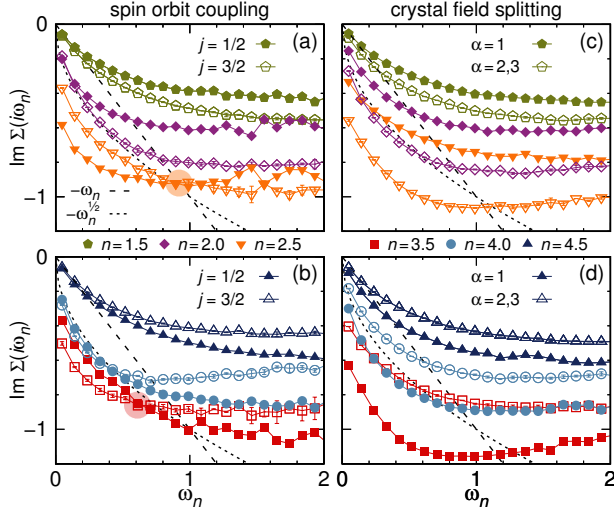


FIG. 3. Imaginary part of the self-energy on the Matsubara axis for the system with (a,b) spin-orbit coupling (SOC) (c,d) crystal-field (CF) splitting. For (c,d), the CF Hamiltonian, $\mathcal{H}_{\text{CF}} = \Delta_{\text{CF}} \sum_{\sigma} n_{1\sigma}$ is introduced instead of \mathcal{H}_{SOC} . The strength of the SOC and the CF are chosen to produce the same noninteracting DOS: $\lambda/D = 0.25$ and $\Delta_{\text{CF}}/D = 0.375$. $U/D = 3.0$, $J_{\text{H}}/U = 0.15$, and $T/D = 0.015$. Solid (open) symbols in (a,b) denote the $j = 1/2$ ($3/2$) results. Solid (open) symbols in (c,d) correspond to $\alpha = 1$ ($\alpha = 2, 3$). For $j = 3/2$ in (a,b) the average over $m_j = \pm 1/2, \pm 3/2$ is shown. In (c,d), we plot the average of $\alpha = 2, 3$ and spin. The shadings in (a,b) highlight the intersections between the different self-energies. The dashed (dotted) lines correspond to $-\omega_n$ ($-\omega_n^{0.5}$) as a guide for the low frequency scaling.

compared to the FL phase.

A remarkable finding is that there exists an intersection between the two self-energies from the different j bands in the NFL phase (see shadings in Fig. 3 (a) and (b)). This intersection implies that the scattering rate near the Fermi-level, $\text{Im}\Sigma(\omega \sim 0)$, and the total scattering rate, $\int_{-\infty}^{\infty} d\omega \text{Im}\Sigma(\omega)$ have different relative magnitudes for the $j = 1/2$ and $3/2$ electrons. For example, for $n = 3.5$, the $j = 3/2$ electrons have a larger value of Γ with larger scattering rate at the Fermi-level, while they exhibit a smaller high energy coefficient of the $1/(i\omega_n)$ tail, implying a smaller total scattering rate. Such a behavior is not observed in the Hubbard model with ordinary crystal field (CF) splitting (no SOC) as shown in Figs. 3 (c) and (d) [38]. We suggest that the basis transformation and corresponding modification of the interaction, especially of the Hund's coupling, are the origin of this phenomenon. This implies that the interplay between spin-orbit coupling effects and electronic correlation cannot be fully captured by an effective crystal-field splitting description. We call this phenomenon spin-orbit-correlation induced flavor selectivity.

Note that the frozen **J**-moment and the NFL behavior are characteristic features of multiorbital systems with large composite moments. Within the **J**-freezing region,

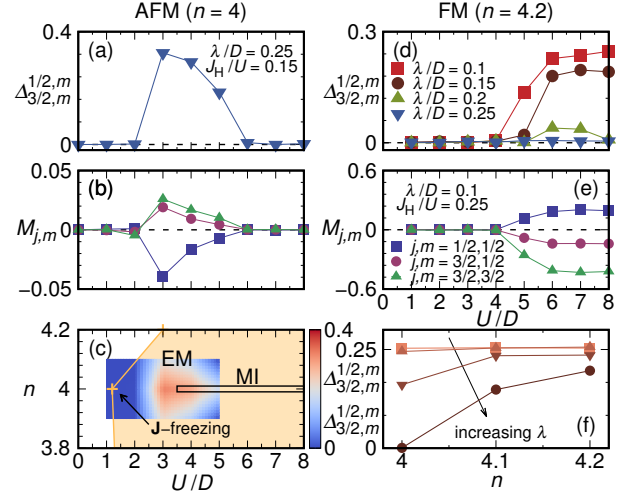


FIG. 4. (a) Excitonic order parameter and (b) magnetic components as a function of U/D at $T/D = 0.33$ for $n = 4.0$, $\lambda/D = 0.25$ and $J_{\text{H}}/U = 0.15$. (c) Density plot for the AFM excitonic order parameter. Here, EM represents the excitonic magnetism. The black bar and yellow line indicate the boundary of the (paramagnetic) metal-insulator (MI) and **J**-freezing regime, respectively. (d) Excitonic order parameter and (e) magnetic components as a function of U/D at $T/D = 0.33$ for $n = 4.2$, $J_{\text{H}}/U = 0.25$ and various λ/D values. (f) Doping dependence of the excitonic order parameter: from top to bottom, corresponding λ/D values are 0.0, 0.05, 0.1, and 0.15, respectively.

even the $j = 1/2$ electrons show NFL behavior, and the single-band description for $j = 1/2$ is not valid anymore. Accordingly, the **J**-freezing crossover line delimits the region of validity of the single-band description.

Besides the paramagnetic phase, we also investigate the excitonic magnetism (EM) near $n = 4$ [10, 12, 13, 39]. To access such a symmetry broken phase, we introduce the off-diagonal components of the Green function and define the order parameter of the exciton condensed phase as $\Delta_{jm}^{j'm'} = \langle c_{jm}^{\dagger} c_{j'm'} \rangle$, where $j' \neq j$. The magnetic components are defined as $M_{j,m} = \langle n_{j,+m} \rangle - \langle n_{j,-m} \rangle$. We find two types of magnetism: Antiferromagnetism (AFM) and ferromagnetism (FM) at different fillings. At $n = 4$ an AFM excitonic state appears at intermediate interaction strength [10, 39–42]. The corresponding region is located around the metal-insulator transition point of the paramagnetic calculations, $U_c/D \sim 3.5$. Figures 4 (a) and (b) show that AFM ($M_{j,m} \neq 0$) and excitonic order ($\Delta_{3/2,m}^{1/2,m} \neq 0$) appear simultaneously. Upon electron doping, the AFM state is rapidly suppressed and eventually vanishes around $n \sim 4.2$, which is shown in Fig. 4(c).

Ba_2YIrO_6 is a d^4 system whose ground state is experimentally not completely resolved [43, 44]. According to the realistic parameter values in Ba_2YIrO_6 as given in Table SV in the supplementary materials (Ref. [26]), we would find a $J = 0$ state in this system.

For large Hund's coupling and small SOC, a FM state emerges in the strong interaction region (Fig. 4(d) and (e)). However, the SOC effectively suppresses the FM state and drives the system into an AFM state at $n = 4$ (see Fig. S5 in Ref. [26]). Compared to the $n = 4$ case, the doped FM state at $n = 4.2$ is less sensitive to the SOC (Fig. 4(f)). We expect that the larger kinetic energy gain for $n > 4$ favors the FM state.

Conclusions. We have explored the paramagnetic phase diagram of the spin-orbit-coupled three-orbital Hubbard model at general filling. We found a generalized **J**-freezing crossover as a function of U , J_H , λ and n which exhibits a strong particle-hole asymmetry and we have detected a metallic phase with a large $\Delta\chi_{\text{loc}}$ near $n = 2$ and a small $\Delta\chi_{\text{loc}}$ near $n = 4$, which is the effect of Hund's third rule on the itinerant phase. Across the **J**-freezing line, a FL-to-NFL crossover appears with a peculiar flavor selectivity in the NFL phase. This is a unique feature of SOC, which is not present in models with ordinary crystal-field splitting. We expect that hole-doping of materials with d^5 filling like iridates or rhodates will shift the systems toward the **J**-freezing line. Near $n = 4$, we observe excitonic magnetism with both AFM and FM order which is consistent with a recent mean-field study [10]. Upon electron doping, the AFM state at $n = 4$ is suppressed and the FM state emerges with enhanced Hund's coupling. These results offer new routes for finding exotic phases by doping $4d$ and $5d$ based materials.

Acknowledgements We thank Ying Li, Steffen Backes, Steve Winter, Ryui Kaneko, Jan Kuneš, Alexander I. Lichtenstein, Jeroen van den Brink, Bernd Büchner, Laura Teresa Corredor Bohorquez, and Gang Cao for helpful discussions. This research was supported by the Deutsche Forschungsgemeinschaft through FOR1346. The computations were performed at Center for Scientific Computing (CSC), the University of Frankfurt.

* aaram@itp.uni-frankfurt.de

- [1] B. Kim, H. Ohsumi, T. Komesu, S. Sakai, T. Morita, H. Takagi, and T. Arima, Phase-sensitive observation of a spin-orbital Mott state in Sr_2IrO_4 , *Science* **323**, 1329 (2009).
- [2] J. Chaloupka, G. Jackeli, G. Khaliullin, Kitaev-Heisenberg model on a honeycomb lattice: Possible exotic phases in iridium oxides A_2IrO_3 , *Phys. Rev. Lett.* **105**, 027204 (2010).
- [3] R. Comin G. Levy, B. Ludbrook, Z.-H. Zhu, C. N. Veenstra, J. A. Rosen, Yogesh Singh, P. Gegenwart, D. Stricker, J. N. Hancock, D. van der Marel, I. S. Elfimov, and A. Damascelli, Na_2IrO_3 as a Novel Relativistic Mott Insulator with a 340-meV Gap, *Phys. Rev. Lett.* **109**, 266406 (2012).
- [4] K. Plumb, J. Clancy, L. Sandilands, V. V. Shankar, Y. Hu, K. Burch, H.-Y. Kee, and Y.-J. Kim, α - RuCl_3 : A spin-orbit assisted Mott insulator on a honeycomb lattice, *Phys. Rev. B* **90**, 041112 (2014).
- [5] S. M. Winter, Y. Li, H. O. Jeschke, and R. Valentí, Challenges in design of Kitaev materials: Magnetic interactions from competing energy scales, *Phys. Rev. B* **93**, 214431 (2016).
- [6] F. Lang, P. J. Baker, A. A. Haghighirad, Y. Li, D. Prabhakaran, R. Valentí, and S. J. Blundell, Unconventional magnetism on a honeycomb lattice in α - RuCl_3 studied by muon spin rotation, *Phys. Rev. B* **94**, 020407 (2016).
- [7] Y. Singh and P. Gegenwart, Antiferromagnetic Mott insulating state in single crystals of the honeycomb lattice material Na_2IrO_3 , *Phys. Rev. B* **82**, 064412 (2010).
- [8] R. D. Johnson, S. C. Williams, A. A. Haghighirad, J. Singleton, V. Zapf, P. Manuel, I. I. Mazin, Y. Li, H. O. Jeschke, R. Valentí, and R. Coldea, Monoclinic crystal structure of α - RuCl_3 and the zigzag antiferromagnetic ground state, *Phys. Rev. B* **92**, 235119 (2015).
- [9] Z. Y. Meng, Y. B. Kim, and H.-Y. Kee, Odd-Parity Triplet superconducting phase in multiorbital materials with a strong spin-orbit coupling: Application to doped Sr_2IrO_4 , *Phys. Rev. Lett.* **113**, 177003 (2014).
- [10] J. Chaloupka and G. Khaliullin, Doping-induced ferromagnetism and possible triplet pairing in d^4 Mott insulators, *Phys. Rev. Lett.* **116**, 017203 (2016).
- [11] W. Witczak-Krempa, G. Chen, Y. B. Kim, and L. Balents, Correlated quantum phenomena in the strong spin-orbit regime, *Annu. Rev. Condens. Matter Phys.* **5**, 57 (2014).
- [12] G. Khaliullin, Excitonic magnetism in Van Vleck-type d^4 Mott insulators, *Phys. Rev. Lett.* **111**, 197201 (2013).
- [13] O. N. Meetei, W. S. Cole, M. Randeria, and N. Trivedi, Novel magnetic state in d^4 Mott insulators, *Phys. Rev. B* **91**, 054412 (2015).
- [14] G. Chen and L. Balents, Spin-orbit coupling in d^2 ordered double perovskites, *Phys. Rev. B* **84**, 094420 (2011).
- [15] G. Chen, R. Pereira, and L. Balents, Exotic phases induced by strong spin-orbit coupling in ordered double perovskites, *Phys. Rev. B* **82**, 174440 (2010).
- [16] O. N. Meetei, O. Erten, M. Randeria, N. Trivedi, and P. Woodward, Theory of high T_c ferrimagnetism in a multiorbital Mott insulator, *Phys. Rev. Lett.* **110**, 087203 (2013).
- [17] H. Shinaoka, S. Hoshino, M. Troyer, and P. Werner, Phase diagram of pyrochlore iridates: All-in-all-out magnetic ordering and non-Fermi-liquid properties, *Phys. Rev. Lett.* **115**, 156401 (2015).
- [18] K. Foyevtsova, H. O. Jeschke, I. I. Mazin, D. I. Khomskii, R. Valentí, Ab initio analysis of the tight-binding parameters and magnetic interactions in Na_2IrO_3 , *Phys. Rev. B* **88**, 035107 (2013).
- [19] J. Kanamori, Electron correlation and ferromagnetism of transition metals, *Prog. Theor. Phys.* **30**, 275 (1963).
- [20] H. Watanabe and T. Shirakawa and S. Yunoki, Microscopic study of a spin-orbit-induced Mott insulator in Ir oxides, *Phys. Rev. Lett.* **105**, 216410 (2010).
- [21] A. Georges, G. Kotliar, W. Krauth, and M. J. Rozenberg, Dynamical mean-field theory of strongly correlated fermion systems and the limit of infinite dimensions, *Rev. Mod. Phys.* **68**, 13 (1996).
- [22] E. Gull, A. J. Millis, A. I. Lichtenstein, A. N. Rubtsov, M. Troyer, and P. Werner, Continuous-time Monte Carlo methods for quantum impurity models, *Rev. Mod. Phys.* **83**, 349 (2011).

- [23] P. Werner and A. J. Millis, Hybridization expansion impurity solver: General formulation and application to Kondo lattice and two-orbital models, *Phys. Rev. B* **74**, 155107 (2006).
- [24] T. Sato, T. Shirakawa, and S. Yunoki, Spin-orbit-induced exotic insulators in a three-orbital Hubbard model with $(t_{2g})^5$ electrons, *Phys. Rev. B* **91**, 125122 (2015).
- [25] S. Hoshino and P. Werner, Superconductivity from emerging magnetic moments, *Phys. Rev. Lett.* **115**, 247001 (2015).
- [26] See Supplemental Material at [URL will be inserted by publisher], which includes Refs. [27–32], for data of **J** correlation function and local susceptibility, the analysis of the local Hamiltonian and the magnetic phases, and the summary of the reported parameter values for various materials.
- [27] M. W. Haverkort, I. S. Elfimov, L. H. Tjeng, G. A. Sawatzky, and A. Damascelli, Strong Spin-Orbit Coupling Effects on the Fermi Surface of Sr_2RuO_4 and Sr_2RhO_4 , *Phys. Rev. Lett.* **101**, 026406 (2008).
- [28] L. Vaugier, H. Jiang, and S. Biermann, Hubbard U and Hund exchange J in transition metal oxides: Screening versus localization trends from constrained random phase approximation, *Phys. Rev. B* **86**, 165105 (2012).
- [29] I. I. Mazin and D. J. Singh, Electronic structure and magnetism in Ru-based perovskites, *Phys. Rev. B* **56**, 2556 (1997).
- [30] K. Pajskr, P. Novák, V. Pokorný, J. Kolorenč, R. Arita, and J. Kuneš, On the possibility of excitonic magnetism in Ir double perovskites, *Phys. Rev. B* **93**, 035129 (2016).
- [31] S. Gangopadhyay and W. E. Pickett, Interplay between spin-orbit coupling and strong correlation effects: Comparison of the three osmate double perovskites Ba_2AOsO_6 ($A = \text{Na}, \text{Ca}, \text{Y}$), *Phys. Rev. B* **93**, 155126 (2016).
- [32] K.-W. Lee and W. E. Pickett, Orbital-quenching-induced magnetism in $\text{Ba}_2\text{NaOsO}_6$, *EPL (Europhysics Letters)* **80**, 37008 (2007).
- [33] P. Werner, E. Gull, M. Troyer, and A. J. Millis, Spin freezing transition and non-Fermi-liquid self-energy in a three-orbital model, *Phys. Rev. Lett.* **101**, 166405 (2008).
- [34] L. de' Medici, J. Mravlje, and A. Georges, Janus-faced influence of Hund's rule coupling in strongly correlated materials, *Phys. Rev. Lett.* **107**, 256401 (2011).
- [35] L. Du, L. Huang and X. Dai, Metal-insulator transition in three-band Hubbard model with strong spin-orbit interaction, *Eur. Phys. J. B* **86**, 1 (2013).
- [36] J. Bünemann, T. Linneweber, U. Löw, F. B. Anders, and F. Gebhard, Interplay of Coulomb interaction and spin-orbit coupling, *arXiv:1603.07544*.
- [37] N. Ashcroft and N. Mermin, *Solid state physics* (Saunders College, Philadelphia, 1976).
- [38] L. de' Medici, S. R. Hassan, M. Capone, and X. Dai, Orbital-selective Mott transition out of band degeneracy lifting, *Phys. Rev. Lett.* **102**, 126401 (2009).
- [39] J. Kuneš, Phase diagram of exciton condensate in doped two-band Hubbard model, *Phys. Rev. B* **90**, 235140 (2014).
- [40] H. Zhang, J. Terizc, F. Ye, P. Schlottmann, H. D. Zhao, S. J. Yuan, G. Cao, Breakdown of the spin-orbit imposed $J_{\text{eff}} = 0$ singlet state in double-perovskite iridates with $\text{Ir}^{5+}(5d^4)$ ions, *arXiv:1608.07624*.
- [41] T. Sato, T. Shirakawa, and S. Yunoki, Spin-orbital entangled excitonic insulators in $(t_{2g})^4$ correlated electron systems, *arXiv:1603.01800v1*.
- [42] S. Hoshino and P. Werner, Electronic orders in multi-orbital Hubbard models with lifted orbital degeneracy, *Phys. Rev. B* **93**, 155161 (2016).
- [43] L. T. Corredor, G. Aslan-Cansever, M. Sturza, K. Manna, A. Maljuk, S. Gass, A. Zimmermann, T. Dey, C. G. F. Blum, M. Geyer, A. U. B. Wolter, S. Wurmehl, and B. Buechner, The iridium double perovskite Sr_2YIrO_6 revisited: A combined structural and specific heat study, *arXiv:1606.05104*.
- [44] T. Dey, A. Maljuk, D. Efremov, V. O. Kataeva, S. Gass, C. G. F. Blum, F. Steckel, D. Gruner, T. Ritschel, A. U. B. Wolter, J. Geck, C. Hess, K. Koepernik, van den J. Brink, S. Wurmehl, and B. Büchner, Ba_2YIrO_6 : A cubic double perovskite material with Ir^{5+} ions *Phys. Rev. B* **93**, 014434 (2016).

Supplemental Information: J-freezing and Hund's rules in spin-orbit-coupled multiorbital Hubbard models

Aaram J. Kim,¹ Harald O. Jeschke,¹ Philipp Werner,² and Roser Valentí¹

¹*Institut für Theoretische Physik, Goethe-Universität Frankfurt,
Max-von-Laue-Straße 1, 60438 Frankfurt am Main, Germany*

²*Department of Physics, University of Fribourg, Chemin du Musée 3, 1700 Fribourg, Switzerland*

J_z correlation function and local susceptibility

In this section, we illustrate the correlation functions which are the basic tool for investigating the phase diagram of the three-band Hubbard model with spin-orbit coupling. Figure S1 presents the local correlation function of the total moment J_z and the corresponding susceptibility for two different fillings, $n = 2$ and 4. Figure 1 in the main text and Fig. S2 are constructed based on these correlation functions. The instantaneous value of the correlation function, $\langle J_z^2 \rangle$, is determined by the size of the local moment and the right most value, $\langle J_z(\beta/2)J_z \rangle$, estimates the long-term memory for a given temperature scale. The local susceptibility χ_{loc} (Eq. (4) in the main text) and its dynamic contribution $\Delta\chi_{\text{loc}}$ (Eq. (5) in the main text) are graphically illustrated in Fig. S1 (a).

In the $n = 2$ case, the correlation function and the susceptibility show a monotonic behavior. As strong Coulomb interactions localize the electrons, both the size of the local moment and its long-term memory increase simultaneously. The increase in both quantities contributes to the susceptibility. However, the dynamic contribution shows a peak at an intermediate interaction value (Fig. S1 (c)). Compared to the noninteracting limit, the enhanced correlations and slow decay of the moment result in a larger value of $\Delta\chi_{\text{loc}}$, but this quantity again vanishes in the fully localized

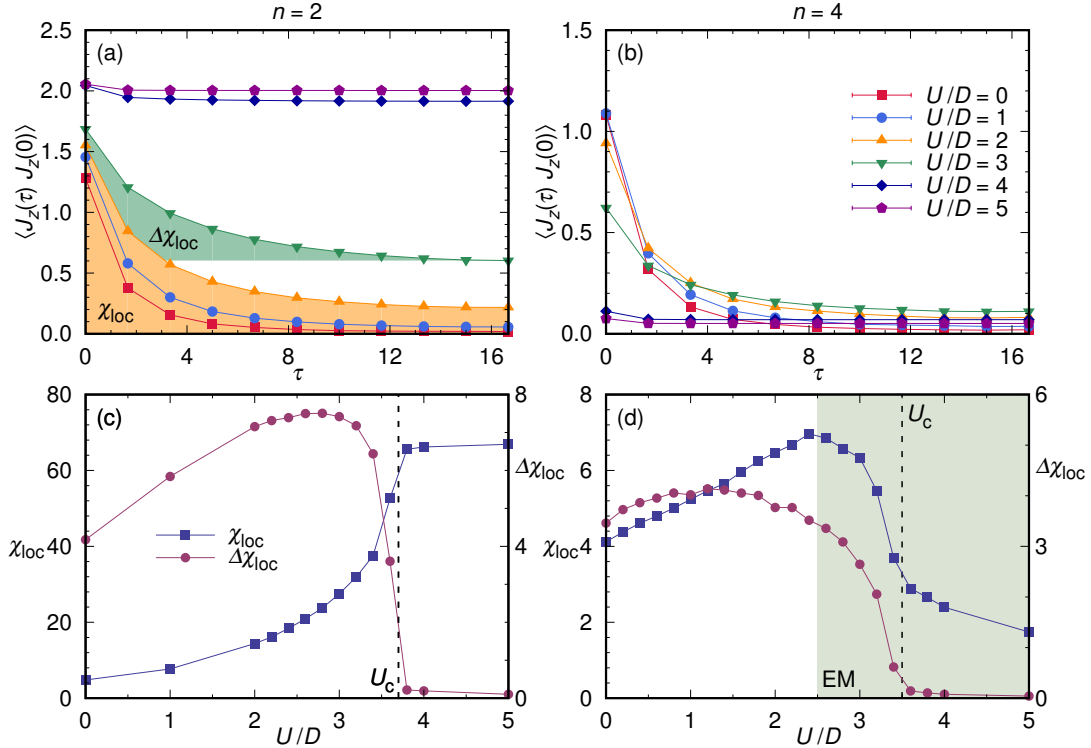


Figure S1: (a), (b) Dynamical correlation function of the total moment J_z for various U/D values. (c,d) The susceptibility and its dynamical contribution as a function of U/D . (c), (d) The vertical dashed lines mark the critical interaction strength U_c of the metal-insulator-transition. The green shading in (d) represents the excitonic AFM region. The left and right columns show the $n = 2$ and $n = 4$ results, respectively. $\lambda/D = 0.25$, $J_H/U = 0.15$, and $T/D = 0.03$ for all panels. The color scheme is fixed within the same row. χ_{loc} and $\Delta\chi_{\text{loc}}$ are graphically represented in panel (a).

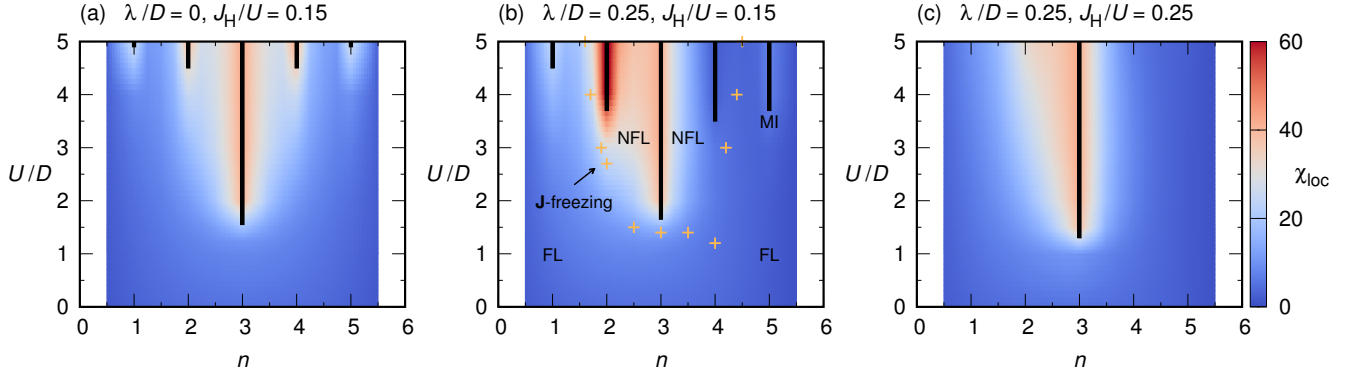


Figure S2: Local susceptibility in the $(U/D, n)$ phase diagram for (a) $\lambda/D = 0.0$, $J_H/U = 0.15$, (b) $\lambda/D = 0.25$, $J_H/U = 0.15$, (c) $\lambda/D = 0.25$, $J_H/U = 0.25$, and $T/D = 0.03$. Cross symbols mark the maximum values of $\Delta\chi_{\text{loc}}$ (compare Figs. S1 (c) and (d)) which may be used to define the **J**-freezing crossover points.

limit. Hence, a peak in $\Delta\chi_{\text{loc}}$ can be naturally expected as a function of U .

On the other hand, the behavior of the local susceptibility is nonmonotonic in the $n = 4$ case. The long-term memory of the correlation function and the susceptibility show a peak structure in the intermediate interaction regime. The strong suppression of the susceptibility in the localized phase, which may be attributed to the nonmagnetic character of the Van-Vleck-type ground state (vanishing **J**-moments) leads to this peak structure. The form of the ground state is shown in Table SII. In other words, the small peak in χ_{loc} is the result of a competition between **J**-freezing and quenching of the local moment. If symmetry breaking is allowed, the antiferromagnetic and excitonic order extend into the region with enhanced local spin susceptibility. In this sense, we may regard the fluctuating local moments in this crossover regime as the hosting background for the symmetry-broken states.

The very different behaviors of the susceptibility in the $n = 2$ and 4 cases are illustrated in Fig. S2. Compared to the non-spin-orbit-coupled system, Fig. S2 (a), the enhancement at $n = 2$ and the suppression at $n = 4$ of the local susceptibility in and near the localized phase are clearly evident in Fig. S2 (b). These strong effects persist into the intermediate coupling regime and for doped systems, as shown in Figs. S2 (b) and (c). The susceptibility of the itinerant phase with $n = 2$ is much larger than for $n = 4$.

It is interesting to analyze the different contributions to the total moment correlation function in the **J**-freezing region. The correlation function of the J_z -moment can be expressed as

$$\langle J_z(\tau)J_z(0) \rangle = \langle L_z(\tau)L_z(0) \rangle + \langle S_z(\tau)S_z(0) \rangle + \langle L_z(\tau)S_z(0) \rangle + \langle S_z(\tau)L_z(0) \rangle. \quad (1)$$

Figure S3 shows the J_z -correlation function and its individual terms for several different fillings. When considering fillings which are symmetric relative to $n = 3$, for example $n = 2$ and 4 (or $n = 2.5$ and 3.5), one notices that the difference in the J_z -correlations function mainly comes from the opposite sign in the L_z - S_z contributions. On the other hand, the L_z - and S_z -correlation functions are very similar for both fillings.

As the system gets closer to half-filling, the contribution of the S_z -correlation function increases while that of the L_z and L_z - S_z correlation function is suppressed. The dominant contribution of the S_z correlation function at $n = 2.5$ and 3.5 can be attributed to the effect of the atomic ground state at $n = 3$ with a spin-maximized and orbital-singlet state. This analysis suggests that the flavor-averaged value of the scattering rate at the Fermi-level is mostly determined by the spin correlation function and that the similar values of the dominant S_z -correlation function for symmetric fillings result in similar values of the average scattering rate. This is indeed the case as can be seen in Fig. 3 of the main text.

Local Hamiltonian

The local Hamiltonian not only describes the physical properties of the fully localized limit but also affects the properties of the correlated itinerant phases. In our model, the local Hamiltonian is composed of two terms: the SOC and the Kanamori-type Coulomb interaction,

$$\mathcal{H}_{\text{loc}} = \mathcal{H}_{\lambda} + \mathcal{H}_{\text{int}}. \quad (2)$$

Using the total electron number N and the total moment J_z as quantum numbers, we diagonalized \mathcal{H}_{loc} . Tables SI and SII summarize the properties of the ground states for each N . In Table SI, the numbers in parenthesis are the

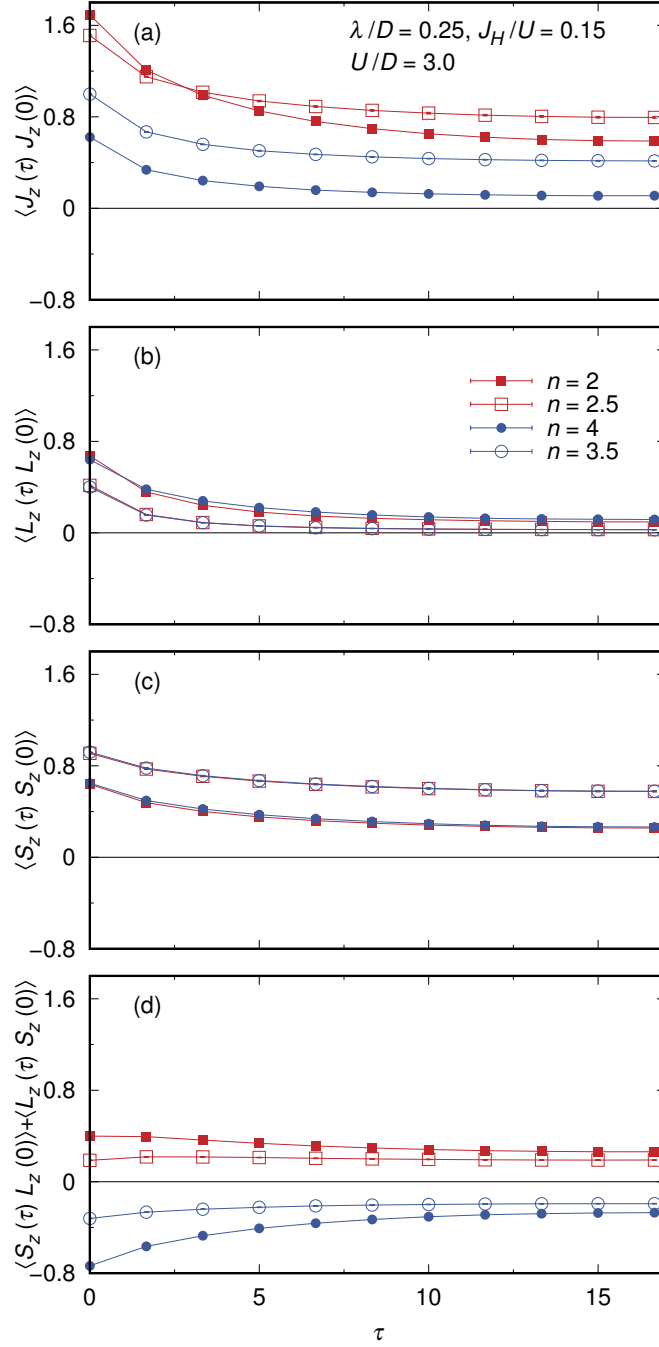


Figure S3: Various correlation functions for $\lambda/D = 0.25$, $J_H/U = 0.15$, $U/D = 3$, and $T/D = 0.03$. From top to bottom, the corresponding functions are the auto-correlation functions of the J_z , L_z , and S_z moment, and the cross-correlation function between the S_z and L_z moment.

ground state degeneracies of the non-spin-orbit-coupled Hamiltonian and μ is the chemical potential. As we turn on the SOC, the degeneracy is reduced except for $N = 3$, which means that the average kinetic energy is reduced, as discussed in the main text. Based on the ground state energy, we calculate the charge gap, defined by

$$\Delta_{\text{ch}}(N) = (E_g(N+1) - E_g(N)) - (E_g(N) - E_g(N-1)) , \quad (3)$$

where $E_g(N)$ is the ground state energy of the local Hamiltonian for filling N . The results are summarized in Table SIII, and Fig. S4 represents $\delta\Delta_{\text{ch}}(N, J_H, \lambda) \equiv \Delta_{\text{ch}} - U$. The summary of the Hund's rules which apply to the local Hamiltonian is also presented in Table SIV.

N	Degeneracy	Ground State Energy (E_g)
0	1 (1)	0
1	4 (6)	$-\frac{\lambda}{2} - \mu$
2	5 (9)	$\frac{1}{4} \left(4U - 8J_H - \lambda - \sqrt{16J_H^2 + 8J_H\lambda + 9\lambda^2} \right) - 2\mu$
3	4 (4)	$3U + f(J_H, \lambda) - 3\mu$
4	1 (9)	$\frac{1}{2} \left(12U - 21J_H - \lambda - \sqrt{25J_H^2 + 10J_H\lambda + 9\lambda^2} \right) - 4\mu$
5	2 (6)	$10U - 20J_H - \lambda - 5\mu$
6	1 (1)	$15U - 30J_H - 6\mu$

Table SI: Ground state energy and degeneracy of the local Hamiltonian for different total particle numbers. The numbers in the parentheses show the ground state degeneracies when $\lambda = 0$.

N	J_z	Ground State
1	+3/2	
	+1/2	
	-1/2	
	-3/2	
2	+2	$\alpha \left(\begin{array}{c} \text{Diagram 1} \\ \text{Diagram 2} \end{array} \right) - \beta \left(\begin{array}{c} \text{Diagram 3} \\ \text{Diagram 4} \end{array} \right)$
	+1	$\alpha \left(\begin{array}{c} \text{Diagram 5} \\ \text{Diagram 6} \end{array} \right) - \beta \left(\begin{array}{c} \text{Diagram 7} \\ \text{Diagram 8} \end{array} \right) - \gamma \left(\begin{array}{c} \text{Diagram 9} \\ \text{Diagram 10} \end{array} \right)$
	0	$\alpha \left(\left(\begin{array}{c} \text{Diagram 11} \\ \text{Diagram 12} \end{array} \right) + \left(\begin{array}{c} \text{Diagram 13} \\ \text{Diagram 14} \end{array} \right) \right) + \beta \left(\left(\begin{array}{c} \text{Diagram 15} \\ \text{Diagram 16} \end{array} \right) - \left(\begin{array}{c} \text{Diagram 17} \\ \text{Diagram 18} \end{array} \right) \right)$
	-1	$\alpha \left(\begin{array}{c} \text{Diagram 19} \\ \text{Diagram 20} \end{array} \right) + \beta \left(\begin{array}{c} \text{Diagram 21} \\ \text{Diagram 22} \end{array} \right) + \gamma \left(\begin{array}{c} \text{Diagram 23} \\ \text{Diagram 24} \end{array} \right)$
3	+3/2	$\alpha \left(\begin{array}{c} \text{Diagram 25} \\ \text{Diagram 26} \end{array} \right) - \beta \left(\begin{array}{c} \text{Diagram 27} \\ \text{Diagram 28} \end{array} \right) - \gamma \left(\begin{array}{c} \text{Diagram 29} \\ \text{Diagram 30} \end{array} \right) - \delta \left(\begin{array}{c} \text{Diagram 31} \\ \text{Diagram 32} \end{array} \right)$
	+1/2	$\alpha \left(\begin{array}{c} \text{Diagram 33} \\ \text{Diagram 34} \end{array} \right) - \beta \left(\begin{array}{c} \text{Diagram 35} \\ \text{Diagram 36} \end{array} \right) - \gamma \left(\begin{array}{c} \text{Diagram 37} \\ \text{Diagram 38} \end{array} \right) + \delta \left(\begin{array}{c} \text{Diagram 39} \\ \text{Diagram 40} \end{array} \right) + \left(\begin{array}{c} \text{Diagram 41} \\ \text{Diagram 42} \end{array} \right) + \left(\begin{array}{c} \text{Diagram 43} \\ \text{Diagram 44} \end{array} \right)$
	-1/2	$\alpha \left(\begin{array}{c} \text{Diagram 45} \\ \text{Diagram 46} \end{array} \right) - \beta \left(\begin{array}{c} \text{Diagram 47} \\ \text{Diagram 48} \end{array} \right) + \gamma \left(\begin{array}{c} \text{Diagram 49} \\ \text{Diagram 50} \end{array} \right) + \delta \left(\begin{array}{c} \text{Diagram 51} \\ \text{Diagram 52} \end{array} \right) + \left(\begin{array}{c} \text{Diagram 53} \\ \text{Diagram 54} \end{array} \right) + \left(\begin{array}{c} \text{Diagram 55} \\ \text{Diagram 56} \end{array} \right)$
	-3/2	$\alpha \left(\begin{array}{c} \text{Diagram 57} \\ \text{Diagram 58} \end{array} \right) + \beta \left(\begin{array}{c} \text{Diagram 59} \\ \text{Diagram 60} \end{array} \right) + \gamma \left(\begin{array}{c} \text{Diagram 61} \\ \text{Diagram 62} \end{array} \right) + \delta \left(\begin{array}{c} \text{Diagram 63} \\ \text{Diagram 64} \end{array} \right) + \left(\begin{array}{c} \text{Diagram 65} \\ \text{Diagram 66} \end{array} \right) + \left(\begin{array}{c} \text{Diagram 67} \\ \text{Diagram 68} \end{array} \right)$
4	0	$\alpha \left(\begin{array}{c} \text{Diagram 69} \\ \text{Diagram 70} \end{array} \right) + \beta \left(\left(\begin{array}{c} \text{Diagram 71} \\ \text{Diagram 72} \end{array} \right) + \left(\begin{array}{c} \text{Diagram 73} \\ \text{Diagram 74} \end{array} \right) \right)$
5	+1/2	
	-1/2	

Table SII: Ground state for a given sector of the local Hamiltonian. In our notation, the upper (lower) level represents the $j = 1/2$ ($3/2$) states and the lower left (right) level corresponds to $m_j = \pm 1/2$ ($m_j = \pm 3/2$). Full (empty) circles mark the positive (negative) m_j electron. All coefficients can be chosen to be real and duplicated symbols in different sectors have nothing to do with each other.

Figures S4 (b) through (f) illustrate the effect of the SOC on the charge gap, which turns out to be different for different N . In the regime of interest, finite J_H and relatively small λ , $\delta\Delta_{\text{ch}}$ is an increasing function of λ for $N = 1, 2$ and 4 , but a decreasing function for $N = 3$ and 5 . Based on the information of the degeneracy and charge gap, we discuss the qualitative behavior of the critical interaction strength U_c in the main text.

N	Charge Gap (Δ_{ch})
1	$U - 2J_H + \frac{3\lambda}{4} - \frac{1}{4}\sqrt{16J_H^2 + 8J_H\lambda + 9\lambda^2}$
2	$f(J_H, \lambda) + U + 4J_H + \frac{1}{2}\sqrt{16J_H^2 + 8J_H\lambda + 9\lambda^2}$
3	$U - \frac{25J_H}{2} - \frac{3\lambda}{4} - \frac{1}{4}\sqrt{16J_H^2 + 8J_H\lambda + 9\lambda^2} - \frac{1}{2}\sqrt{25J_H^2 + 10J_H\lambda + 9\lambda^2} - 2f(J_H, \lambda)$
4	$f(J_H, \lambda) + U + J_H + \sqrt{25J_H^2 + 10J_H\lambda + 9\lambda^2}$
5	$U - \frac{J_H}{2} - \frac{\lambda}{2} - \frac{1}{2}\sqrt{25J_H^2 + 10J_H\lambda + 9\lambda^2}$

Table SIII: Charge gap for different total particle numbers. Note that Δ_{ch} can be expressed as $U + \delta\Delta_{\text{ch}}(N, J_H, \lambda)$. We do not specify $f(J_H, \lambda)$ because it is difficult to express it in a simple form. Numerical values are used to obtain Fig. S4.

n	S	L	J
1	1/2	1	3/2
2	1	1	2
3	3/2	0	3/2
4	1	1	0
5	1/2	1	1/2

Table SIV: Summary of Hund's rules including the third law.

Energy Scales in Various Materials

In Tab. SV, we summarize the previous estimates of the energy scales for various materials. Our main parameter set is chosen to be the estimate from Sr_2IrO_4 [1]. The absolute value of the SOC is mainly determined by the relevant atom; 0.1~0.2 eV for Ru, Rh and 0.3~0.4 eV for Os, Ir. In these materials, the Hund's coupling strength J_H/U varies within 0.1~0.22 which is the range considered in our calculations.

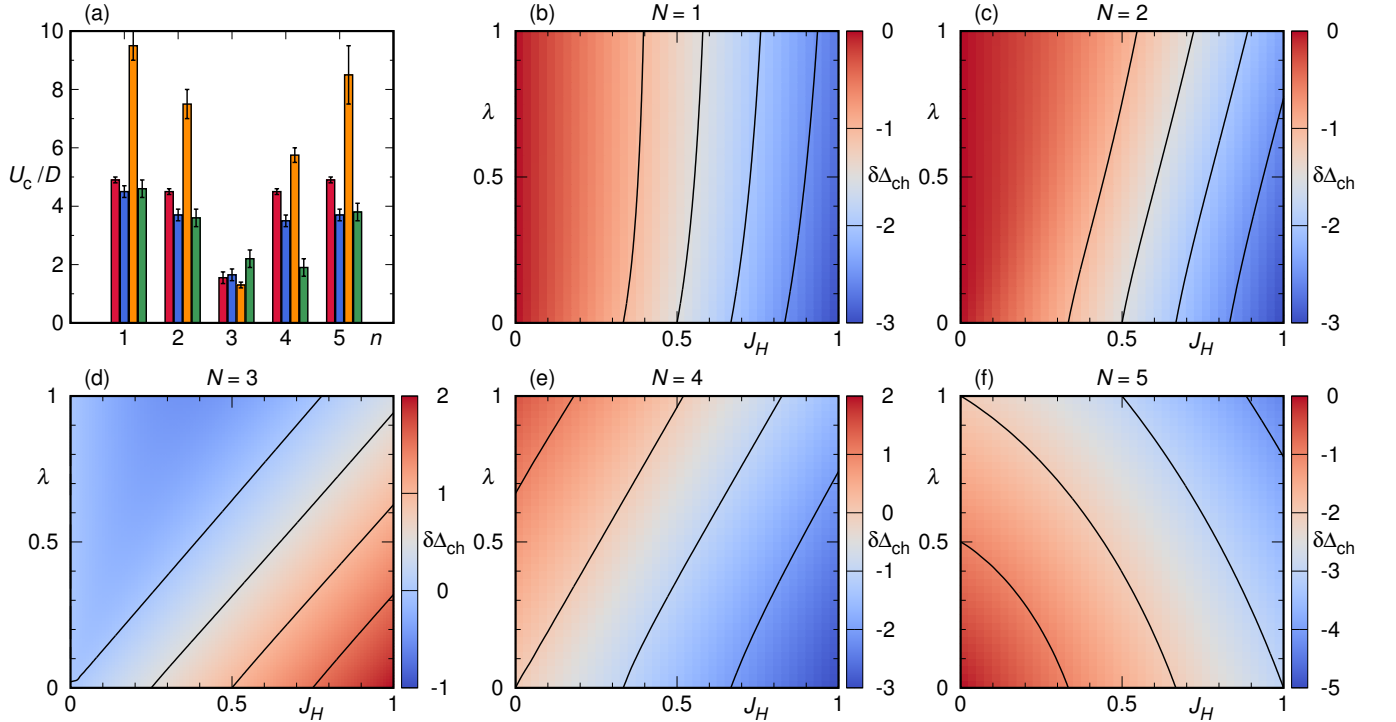


Figure S4: (a) Critical interaction strength U_c as a function of electron filling. From left to right within a group of four bars, the bars represents the U_c for $(\lambda, J_H/U) = (0, 0.15), (0.25, 0.15), (0.25, 0.25),$ and $(0.5, 0.15)$, respectively.

(b)-(f) Density plot of $\delta\Delta_{\text{ch}}$ as a function of J_H and λ for different total particle number N . $\delta\Delta_{\text{ch}}(N, J_H, \lambda)$ is defined as $\Delta_{\text{ch}} - U$.

Material	Conf.	D	λ/D	J_H/U	U/D	Ref.
Sr_2IrO_4	d^5	1.44eV	0.257 (0.37eV)	0.15	-	[1]
Sr_2RhO_4	d^5	1.44eV	0.125 (0.18eV)	0.15	-	[1]
$\text{Y}_2\text{Ir}_2\text{O}_7$	d^5	0.5eV	0.8 (0.4eV)	0.1	5.0 (2.5eV)	[2]
Na_2IrO_3	d^5	0.2eV	2.0 (0.4eV)	0.2	15 (3eV)	[3]
Li_2IrO_3			0.75 (0.15eV)			
$\alpha\text{-RuCl}_3$						
Sr_2RuO_4	d^4	0.75eV	0.13 (0.100eV)	-	-	[4]
Sr_2YRuO_6	d^4	0.55eV	0.18 (0.100eV)	0.20	4.73 (2.6eV)	[5–7]
Sr_2YIrO_6	d^4	0.5eV	0.6 (0.33eV)	0.22	3.6 (1.8eV)	[8]
Ba_2YIrO_6						
$\text{Sr}_2\text{CrOsO}_6$	d^3	0.75eV	0.4 (0.3eV)	0.17	2.67 (2eV)	[9]
$\text{Ba}_2\text{NaOsO}_6$	d^1	0.3eV	1.0 (0.3eV)	-	-	[10, 11]

Table SV: Summary of the energy scales in various spin-orbit-coupled materials. D , λ , J_H , and U are the half-bandwidth, strength of spin-orbit coupling, Hund’s coupling, and Coulomb interaction, respectively.

Long-Range Order near $n = 4$

For large Hund’s coupling and small SOC, we observe itinerant FM. In Fig. S5, the increase of the SOC results in successive phase transitions from FM to AFM, and from AFM to PM. For a given total moment $\langle \mathbf{J} \rangle$, the internal structure is different depending on the magnetic phase. In the FM phase, $\langle \mathbf{S} \rangle$ and $\langle \mathbf{L} \rangle$ are aligned in the same direction, and $\langle \mathbf{S} \rangle$ makes the dominant contribution to $\langle \mathbf{J} \rangle$. On the other hand, in the AFM phase, $\langle \mathbf{S} \rangle$ and $\langle \mathbf{L} \rangle$ are anti-aligned, but $\langle \mathbf{L} \rangle$ dominates $\langle \mathbf{S} \rangle$.

Our results show that the Hund’s coupling enhances the FM while the SOC suppresses it. This behavior is consistent with the previous results [5, 12], especially two-site Exact diagonalization (ED) results in Fig. S6. Assuming a square lattice, the value of the critical strength of the SOC, $\lambda_c/D = 0.1275$ for $J_H/D = 0.25$ in the ED results is compatible with our DMFT results.

-
- [1] H. Watanabe, T. Shirakawa, and S. Yunoki, Phys. Rev. Lett. **105**, 216410 (2010).
 - [2] H. Shinaoka, S. Hoshino, M. Troyer, and P. Werner, Phys. Rev. Lett. **115**, 156401 (2015).
 - [3] S. M. Winter, Y. Li, H. O. Jeschke, and R. Valentí, Phys. Rev. B **93**, 214431 (2016).
 - [4] M. W. Haverkort, I. S. Elfimov, L. H. Tjeng, G. A. Sawatzky, and A. Damascelli, Phys. Rev. Lett. **101**, 026406 (2008).
 - [5] O. N. Meetei, W. S. Cole, M. Randeria, and N. Trivedi, Phys. Rev. B **91**, 054412 (2015).
 - [6] L. Vaugier, H. Jiang, and S. Biermann, Phys. Rev. B **86**, 165105 (2012).
 - [7] I. I. Mazin and D. J. Singh, Phys. Rev. B **56**, 2556 (1997).
 - [8] K. Pajskr, P. Novák, V. Pokorný, J. Kolorenč, R. Arita, and J. Kuneš, Phys. Rev. B **93**, 035129 (2016).
 - [9] O. N. Meetei, O. Erten, M. Randeria, N. Trivedi, and P. Woodward, Phys. Rev. Lett. **110**, 087203 (2013).
 - [10] S. Gangopadhyay and W. E. Pickett, Phys. Rev. B **93**, 155126 (2016).
 - [11] K.-W. Lee and W. E. Pickett, EPL (Europhysics Letters) **80**, 37008 (2007).
 - [12] J. Chaloupka and G. Khaliullin, Phys. Rev. Lett. **116**, 017203 (2016).

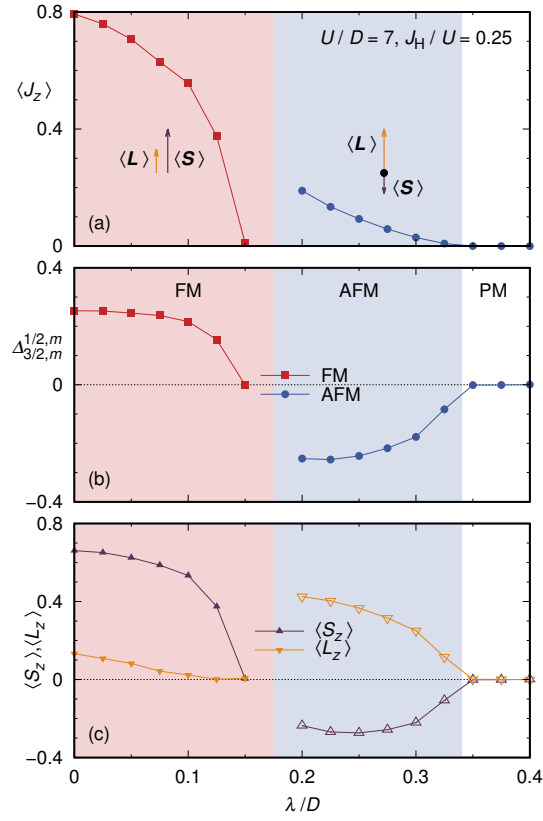


Figure S5: (a) Total magnetic moment, (b) excitonic order parameter and (c) spin/orbital moment as a function of λ/D for $T/D = 0.33$, $n = 4$, $J_H/U = 0.25$, and $U/D = 7$. The red (blue) shading represents the FM (AFM) region. The arrows in (a) show the alignment (anti-alignment) of spin and orbital moment in the FM (AFM) region.

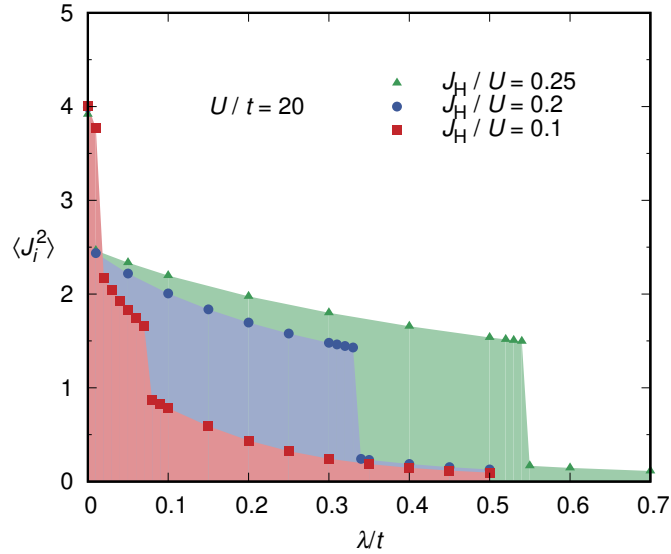


Figure S6: The size of the total moment for a given site in the two-site Hubbard model as a function of λ/t for $U/t = 20$. Here t is the hopping parameter between two sites. From top to bottom, the corresponding Hund's coupling strengths are 0.25, 0.2, and 0.1, respectively.